How to cite: *Angew. Chem. Int. Ed.* **2025**, e18519
doi.org/10.1002/anie.202518519

CO_2 Electroreduction

Lattice Hydrogen Participation and Mass Transport Acceleration Improve CO_2 Electroreduction to C_2 Products

He Zhang+, Simeng Liu+, Chao Zhang+, Wei Liu, Hongliang Dong, Zhaolin Shi, Han Xu, Jinbiao Liu, Dingsheng Wang, Jiqing Jiao, Mingbin Gao,* and Tongbu Lu**

Abstract: CO_2 electroreduction operated at high current densities typically face the critical issues of CO_2 depletion and competing reactions. Here we prepared CuH branched nanosheets stabilized with holmium single atoms (HoSA-CuH). Finite-element analyses show that the branched HoSA-CuH structure could accelerate mass transport and alleviate CO_2 depletion under high current densities. In situ spectroscopies and theoretical calculations reveal that the introduced Ho single atoms increase the electron density at Cu surface, which is conducive to CO_2 enrichment and activation. Deuterium isotope labeling experiments confirm that the lattice hydrogen in CuH participate in the reaction, thereby lowering the energy barrier for the rate-determining step in C–C coupling. Therefore, the selectivity for C_{2+} over HoSA-CuH is above 80% under 700–1200 mA cm^{-2} and C_2 products account for 95% of all the C_{2+} products. Compared with the best-performing catalysts reported thus far, HoSA-CuH displays the broadest current density range for high FE_{C2}.

Introduction

CO_2 electroreduction (CO_2RR) integrated with renewable energy stands as a promising route to converting CO_2 into value-added chemicals under ambient conditions and electrocatalysts with high performances (in particular, at high current densities) play a key role in the implementation of such technologies for industrial applications.[1–3] Yet renewable energies such as solar and wind typically show intermittency and fluctuations and thus it requires the electrocatalysts with high selectivity to be well adapted to a wide range of voltages and current densities.[4] As for the electroreduction products, multi-carbon ones (C_{2+}) generally feature higher profitability than C_1 products; however, generating C_{2+} products involves the complex processes of CO_2 activation, formation of multiple intermediates, and carbon–carbon (C–C) coupling, accompanied by multiple steps of electron/proton transfer.[5–9] In comparison, water dissociation usually has faster kinetics for electron transfer, and the rapidly generated protons may prefer the competing H_2 evolution reaction (HER).[10] In particular, under high current densities, the $CO_2(aq)$ species at the catalytic interface tends to be depleted owing the low solubility and diffusivity of CO_2 in aqueous media, leading to high overpotentials, low catalytic activities, and low selectivities for C_{2+}.[11,12]

Copper (Cu)-based catalysts have been identified as the most promising candidates for generating C_{2+} products via CO_2RR.[13,14] Zeng et al. prepared a series of phosphorus(P)-doped Cu catalysts for CO_2 electroreduction into C_{2+} products. The introduction of P could stabilize the surface $Cu^{\delta+}$ species, enhancing the activity for C_{2+} production[15] Wang et al. reported a fluorine(F)-modified Cu catalyst that exhibits a C_{2+} Faradaic efficiency (FE) of 80% in flow cell[16] Wang et al. demonstrated a benzimidazole-based Cu coordination polymer to enhance CO_2 reduction to C_{2+} products, with the highest FE for C_{2+} products reaching>70% at 260 mA cm^{-2}.[10] Xiong et al. reported that doping potassium(K) in Cu_2Se nanosheet arrays could tune the interaction between Cu sites and reaction intermediates, enabling highly selective production of ethanol[17] Wang et al. synthesized the Cu_3N-Ag nanocubes and the FE for C_2H_4 over catalyst is 7.8 times higher than over Cu_3N.[18] Qiao et al. reported a Ag-modified copper oxide catalyst that exhibits a substantial FE of 40.8% for ethanol under a current density of 326.4 mA cm^{-2}.[19] Cao et al. developed an effective

---

[*] H. Zhang+, S. Liu+, C. Zhang+, Z. Shi, H. Xu, J. Liu, J. Jiao, T. Lu
MOE International Joint Laboratory of Materials Microstructure, Institute for New Energy Materials and Low Carbon Technologies, Analysis and Testing Center, School of Materials Science and Engineering, Tianjin University of Technology, Tianjin 300384, China
E-mail: jiaojiqing101@163.com
lutongbu@tjut.edu.cn

W. Liu
School of Chemistry, State Key Laboratory of Fine Chemicals, Frontier Science Center for Smart Materials, Dalian University of Technology, Dalian 116024, China

H. Dong
Center for High Pressure Science and Technology Advanced Research, Shanghai 201203, China

D. Wang
Department of Chemistry, Tsinghua University, Beijing 100084, China

M. Gao
State Key Laboratory of Physical Chemistry of Solid Surfaces, College of Chemistry and Chemical Engineering, Xiamen University, Xiamen 361005, China
E-mail: mbgao@xmu.edu.cn

[+] These authors contributed equally to this work.

Additional supporting information can be found online in the Supporting Information section tandem catalysis strategy and improved the selectivity for C_2H_4 by multiple distinct catalytic sites in local vicinity[20] Han et al. designed gadolinium-doped CuO_x catalysts; the distinctive electronic structure and large ion radius of Gd help to keep the Cu^+ species stable during the reaction, resulting in excellent performance for electroreduction from CO_2 to C_{2+} products.[21] For most of the conventional Cu-based catalysts catering to CO_2RR, proton transfer is involved in the formation of almost all intermediates and the protons usually come from the activation and dissociation of solvent water or surface-adsorbed water.[22–26] It could be expected that an ill-balanced supply of active hydrogen would either limit the efficiency of converting CO_2 to multi-carbon products, or lead to severe competition from parasitic HER. Such obstacles may be overcome by introducing an alternative way of active hydrogen supply, for example, lattice hydrogens from the electrocatalyst itself. Yet no such systems have been reported thus far, probably because copper hydride (CuH) nanocrystals could hardly be obtained via conventional methods.

In this work, we prepared CuH branched nanosheets stabilized by holmium (Ho) single atoms (denoted as HoSA-CuH). The branched structure of HoSA-CuH brings a microenvironment featuring high local CO_2 concentrations, indicating that HoSA-CuH could well alleviate CO_2 depletion under high current densities. The experimental characterizations show that the single-atomic Ho dopants could not only significantly enhance the stability of CuH, but also alter the crystal structure of CuH and the valence state of Cu, resulting in high-efficiency catalytic sites for C–C coupling. Under the high current densities 700–1200 mA cm^{-2}, the selectivity for C_{2+} is consistently above 80%, and C_2 products (primarily ethylene and ethanol) account for 95% of all the C_{2+} products. In situ spectroscopies and density functional theory (DFT) calculations reveal that the introduction of Ho single atoms leads to a higher electron density at the Cu surface, which is conducive to CO_2 enrichment and activation. Furthermore, deuterium (D) isotope labeling experiments confirm that the lattice hydrogen in CuH participates in the reaction and DFT calculations reveal that these active hydrogen species contribute to *COOH formation, thereby lowering the energy barrier for the rate-determining step (RDS) in C–C coupling. This work not only demonstrates that an alternative source of active hydrogen species could substantially optimize the reaction pathway from CO_2-to-C_{2+} conversion, but also offers a solution to the integration of ampere-level CO_2RR with renewable energy.

Results and Discussion

Synthesis and Characterization of HoSA-CuH

We developed a facile method for the preparation of the Ho-stabilized CuH nanosheets (HoSA-CuH). The synthesis process is illustrated in Figure 1a and the experimental details are summarized in the Methods. In brief, $CuSO_4{\cdot}5H_2O$ and $HoCl_3{\cdot}6H_2O$ were dissolved the solution of hypophosphorous acid (a strong reducing agent), and then the mixture was heated at 40 °C for 2 h. The solid product was obtained via freeze-drying.

The X-ray diffraction (XRD) patterns were recorded to reveal the crystal structure of different samples (Figure S1). The HoSA-CuH sample shows the main peaks at 35.8°, 41.0°, and 64.4°, which can be attributed to the (100), (101), and (110) planes of the hexagonal CuH (PDF 89–4182) and no diffraction peaks of metallic Cu or Cu oxides were found. For the sample prepared without Ho introduction (denoted as Ho-free sample), the primary XRD peaks are at 43.3°, 50.4° and 74.1° indexed to the (111), (200), and (220) planes of cubic Cu metal (PDF 85–1326).[27] Furthermore, there are no diffraction peaks corresponding to Ho or Ho oxides for HoSA-CuH, indicating that the Ho was atomically dispersed in CuH nanocrystals. Therefore, it could be inferred that the introduction of Ho atoms helped to stabilize the CuH crystals. Figure 1b shows the scanning electron microscopy (SEM) image for HoSA-CuH. The uniform nanosheets were clearly observed, with a thickness around 10 nm. The Ho-free sample displays a similar morphology (Figure S2). The transmission electron microscopy (TEM) image for HoSA-CuH (Figures 1c and 1d) reveals that the thin nanosheets are uniform in morphology and size.[28] Figure 1e shows the corresponding high-resolution TEM (HRTEM) image; the lattice fringe of 2.2 Å at the area highlighted by the orange dashed circle could be indexed to the CuH (101) facet. In contrast, for the Ho-free sample, the lattice fringe 2.1 Å is corresponding to (111) facet of cubic Cu (Figure S3). The results are consistent with the XRD patterns.

Furthermore, the aberration-corrected high-angle annular dark field scanning transmission electron microscopy (HAADF-STEM) images were recorded to identify the atomic Ho dispersion on the nanosheets (Figure 1f). The clear lattice fringe of CuH nanocrystals is in good agreement with HRTEM data. The bright spots highlighted by yellow circles confirm that the Ho atoms are well-dispersed on the CuH nanosheets.[29,30] Figure 1g shows two typical spots of Ho single atoms (top) and corresponding 3D intensity profile (bottom). The energy-dispersive X-ray spectroscopy (EDS) element mapping reveals that Cu and Ho species are evenly distributed over the nanosheets (Figure 1h). The actual loading ratio of Ho is ~2.10 wt%, as determined via inductively coupled plasma optical emission spectrometry (ICP-OES) (Table S1). From the results above, it could be confirmed that the Ho species were atomically dispersed in CuH nanosheets.

Synchrotron-based X-ray absorption fine structure (XAFS) measurements were performed to gain insights into the local structures of the synthesized samples.[27] The Ho L_3-edge X-ray absorption near-edge structure (XANES) profile for HoSA-CuH shows a pronounced white-line peak at ~8077 eV (Figure 2a). Detailed atomic structure information can be extracted from the Fourier transformed (FT) *R*-space, as shown in Figure 2b. HoSA-CuH exhibits a prominent main peak at ~1.90 Å (without phase shift correction), which can be assigned to the first-shell Ho–O path. A minor peak could be found at ~2.70 Å, significantly shorter than that for Ho–Ho coordination peak in Ho powder. Through EXAFS

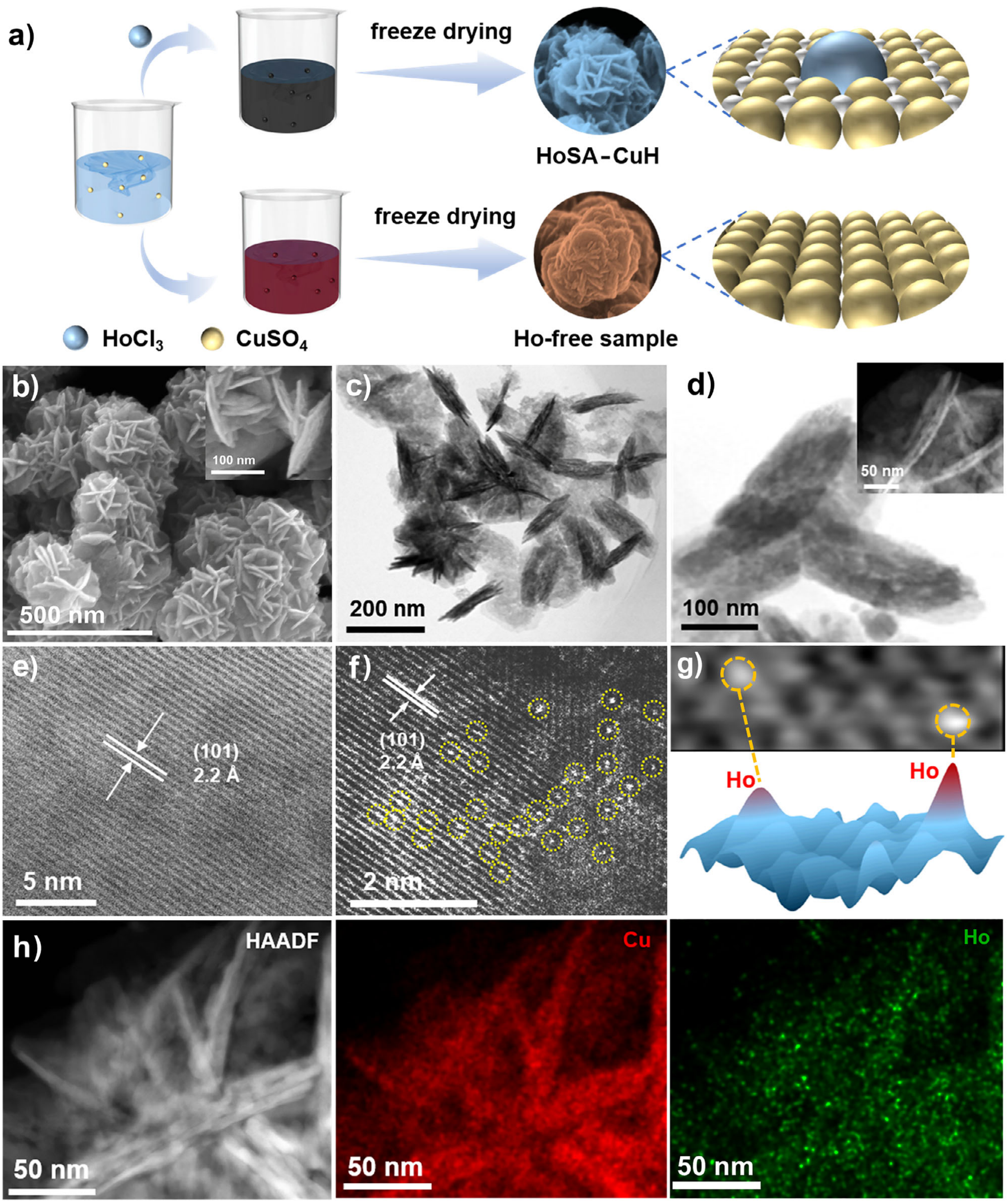

Figure 1. Synthesis and structure characterizations of HoSA-CuH. a) Schematic illustration of the synthesis procedure of HoSA-CuH. b) SEM image. c and d) TEM images. e) HRTEM image. f) HAADF-STEM image. g) Typical spot for Ho single atoms (top), corresponding 3D intensity profiles of HoSA-CuH (bottom). h) EDS mapping.

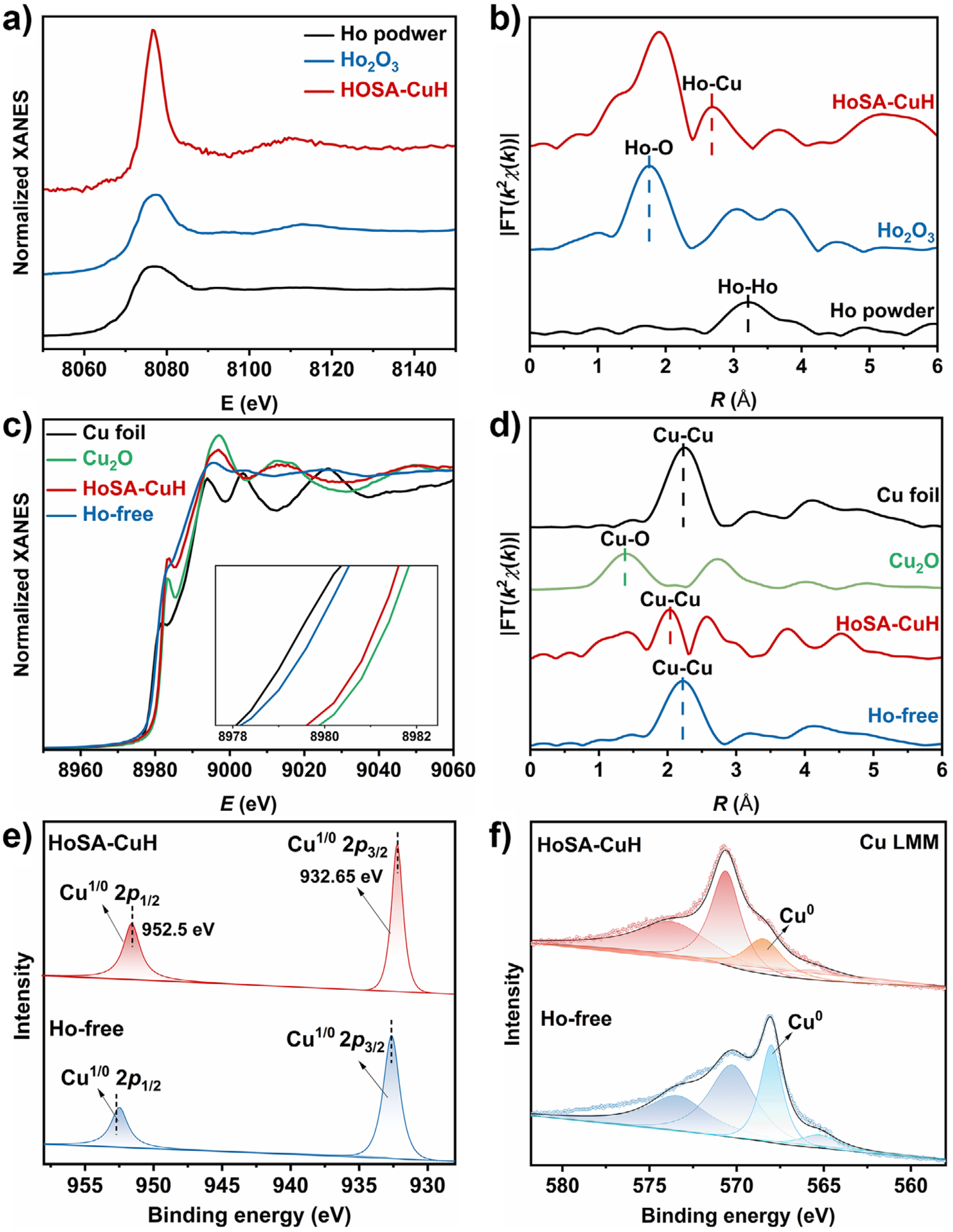

Figure 2. XAFS and XPS data for HoSA-CuH. a and c) Normalized XANES χ (E) spectra for Ho and Cu of HoSA-CuH and other samples. b and d) Radial distance χ (R) space spectra of Ho and Cu. e) High-resolution spectrum for Cu 2*p*. f) Auger LMM spectra spectra for Cu for HoSA-CuH and Ho-free sample.

analysis, this signal can be ascribed to Ho–Cu contribution. Quantitative EXAFS.

Curve -fitting analysis revealed a Ho–Cu coordination number $N = 2.6$. In HoSA-CuH, each Ho atom is coordinated with three Cu atoms on average, probably substituting surface Cu atoms within the CuH lattice (Table S2). The Cu K-edge for XANES was recorded. As shown in Figure 2c and d, the Ho-free Cu display a structure similar to that of Cu.[31,32] Compared with pristine Ho-free Cu, the Cu K-edge XANES for HoSA-CuH displays a distinct positive shift in the absorption edge position, indicating that the valence state of Cu falls between 0 and + 1.[33] This observation is corroborated by the split Cu−Cu peaks spanning 2.0–3.0 Å in *R*-space correspond to metallic and hydrated species. The fitting quantitative χ(R) space and χ(k) spectra were also performed from Figures S4–S9 and Tables S2–S3. This structure is conducive to enhancing C–C coupling in CO_2RR.

The electronic structures and chemical compositions of the two samples were probed via X-ray photoelectron spectroscopy (XPS).[34–36] The survey spectra for HoSA-CuH and free-Ho sample are shown in Figure S10, confirming the presence of the corresponding elements. The signals for Ho 4*d* could not be found in the XPS spectrum (Figure S11), probably owing to the low loading.[37] The high-resolution Cu 2*p* spectra were deconvoluted into two peaks between 933 and 953 eV for Cu^+ or Cu^0, attributed to the Cu $2p_{3/2}$ and

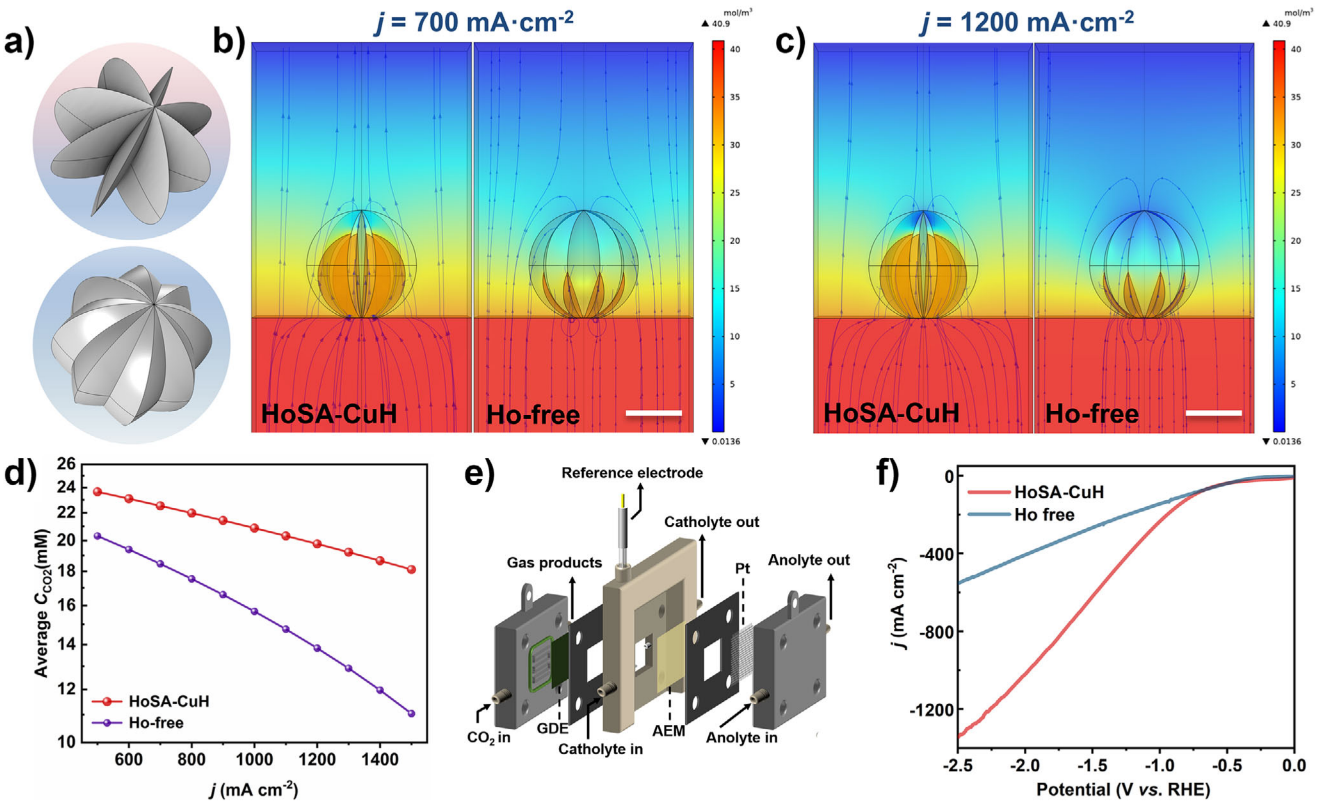

Figure 3. Finite-element analyses and CO_2RR performances. a) Geometric models for HoSA-CuH (top) and Ho-free (bottom) catalysts. b and c) Local CO_2 concentration distributions for the two catalysts at 700 mA cm^{-2} and 1200 mA cm^{-2}. Scale bar: 100 nm. d) Average CO_2 (aq) concentrations at the catalytic interfaces. e) Configuration of flow cell. f) LSV curves without *iR* correction.

Cu 2$p_{1/2}$ peaks, respectively (Figure 2e). In order to estimate the relative ratio of Cu$^+$ and Cu for the two samples, the valence states of Cu in HoSA-CuH and Ho-free sample were evaluated from the Auger LMM spectra from Figure 2f.[34] The proportion of Cu^0 was found to be lower in HoSA-CuH than in Ho-free sample, it could be deduced that the electrons transferred to Cu from Ho due to lower electronegativity. The results of XAS and XPS both confirm the co-existence of Cu^0 and Cu$^+$ in HoSA-CuH, which would be conducive to electrocatalytic CO_2RR for C_{2+} production.

Assessment of CO_2RR Performance

For CO_2RR, mass transport is of particular importance at high current densities. From the electron microscopy images of the HoSA-CuH and Ho-free samples, we noticed that the former consists of branched thin nanosheets, whereas the latter has a walnut-like morphology with shallow wrinkles on the surface. It could thus be postulated that HoSA-CuH would be more advantageous in mass transport. For verification, we conducted finite-element analyses to compare the two catalysts deposited on gas-diffusion layers immersed in aqueous electrolytes. Figure 3a shows the geometric models for the two catalysts, Figure 3b and 3c compare the local concentration distributions of CO_2 for the two systems near the electrode surfaces (at current densities of 700 mA cm^{-2} and 1200 mA cm^{-2}, respectively). It could be clearly seen that the microenvironment for HoSA-CuH always enjoys a higher CO_2 (aq) concentration than the Ho-free counterpart does. Figures S12–S16 summarize the CO_2 concentration distributions at 800–1100 mA cm^{-2}. Figure 3d compares the average CO_2 (aq) concentrations at the catalytic interfaces for the two samples and it could be noted that as the current density increases, the CO_2(aq) concentration around the Ho-free sample declines much more rapidly, indicating that the HoSA-CuH consisting of branched nanosheets could well alleviate CO_2 depletion due to mass transport acceleration, an issue typical for high current densities.

The performance of HoSA-CuH catalysts for CO_2RR was assessed in 1.0 M KOH electrolyte using a three-electrode flow cell, with the hydrophobic HoSA-CuH deposited on carbon paper as the work electrode (Figure S17), Pt as the counter electrode, and Ag/AgCl as the reference electrode[24] (Figure 3f). The details on the flow cell configuration are shown in Figure 3e. Gas chromatography was employed to continuously monitor the gas-phase products (H_2, CO, C_2H_4, etc.) (Figure S18) and the liquid-phase products (formic acid, ethanol, acetate, *n*-propanol, etc.) were analyzed via ^{1}H nuclear magnetic resonance (NMR) spectroscopy (Figure S19). To preliminarily assess the catalysts activity, linear sweep voltammetry (LSV) was performed under CO_2-saturated conditions (Figure S20–S21). The electrochemically active surface areas (ECSAs) of HoSA-CuH and the Ho-free

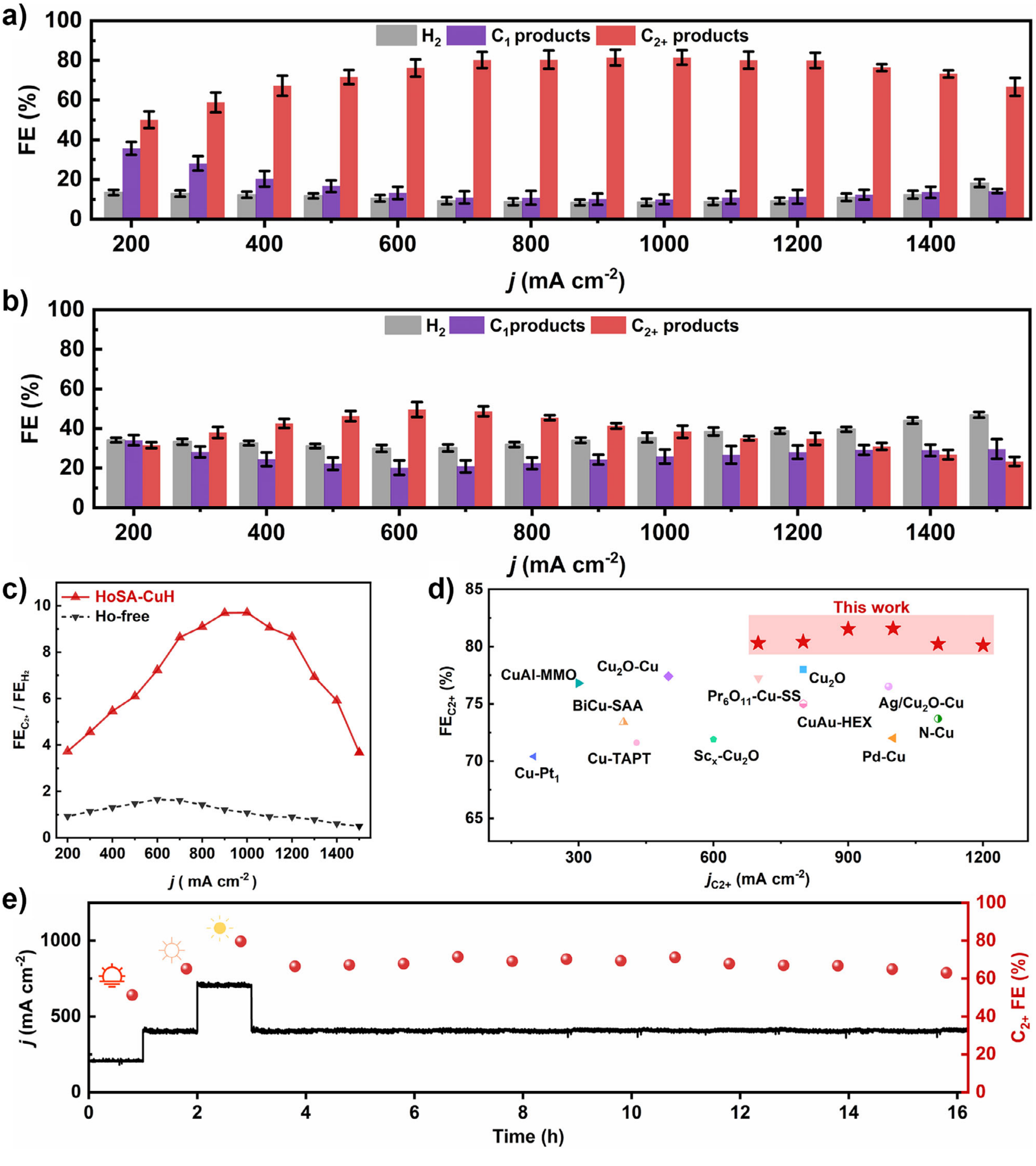

Figure 4. The CO_2RR performances of HoSA-CuH. a) and b) FE for C_{2+} and other products for HoSA-CuH and Ho-free sample under different current density. c) ratio of FE_{C2+}/FE_{H2}. d) Comparison of FE_{C2+} under various current density for reported Ref.[38–49] e) Stability of the flow cell under various current density. The error bars represent the standard deviation of three independent measurements.

sample were measured (Figure S22). As shown in Figure 3f, the HoSA-CuH catalyst displays a higher total current density than the Ho-free sample.

We examined the product selectivities over different samples within the current density range of 200–1500 mA cm^{-2}. As shown in Figure 4a, at the low current density of 200 mA cm^{-2}, the FE for C_{2+} is only 50%; with the current density increasing to 1000 mA cm^{-2}, the FE_{C2+} goes up to 82%; as the current density further increases to 1500 mA cm^{-2}, the FE_{C2+} becomes slightly lower. Yet notably, within the range from 700 mA cm^{-2} to 1200 mA cm^{-2}, the FE_{C2+} is consistently>80%. Figures S23 and S24 summarizes the FEs for all detected products and it could be noted that the C_2 products (primarily ethylene and ethanol) account for 95% of all the C_{2+} products. The competing HER is substantially suppressed; in addition, the selectivities for two-electron reduction products (that is, CO and HCOOH) are also rather low (Figure S25). In stark contrast, for the Ho-free sample from Figure 4b, the FE_{C2+} is significantly lower over the entire range, with a maximum of 49% at 600 mA cm^{-2}, and the competition from HER is rather prominent.

In order to directly compare the preference for producing C_{2+} and H_2 over the two samples, we calculated the FE_{C2+}/FE_{H2} ratios (summarized in Figure 4c). It could be noted that over the range from 700 to 1200 mA cm^{-2}, the FE_{C2+}/FE_{H2} ratio for HoSA-CuH stays above 8.6, with a maximum of ∼10 achieved at 1000 mA cm^{-2}, whereas the the FE_{C2+}/FE_{H2} ratio for Ho-free sample is consistently below 2. These data suggest that HoSA-CuH could ideally catalyze C–C coupling under a broad range of current density at the ampere-per-square-centimeter level. In addition, the various rare-earth elements were doped and samples with different Cu/Ho ratios were analyzed (Figure S26–S27). We compared the operational current densities of some of the best-performing catalysts reported thus far (Figure 4d) and found that our HoSA-CuH features the broadest current density range for high FE_{C2+} (Table S4).[38–49] As shown in Figure 4e, we selected a few typical current densities as the operational parameter to assess the stability of our HoSA-CuH and found that despite the large variation in current density, the catalyst displayed a high FE_{C2+} and a high durability, running for 16 h with barely any decline in performance (Figures S28–S30).[50]

The Catalytic Mechanism of HoSA-CuH

Density functional theory (DFT) calculations were carried out to understand the origins of the high selectivity from CO_2-to-C_{2+} conversion over the HoSA-CuH catalyst. It was found that the introduction of Ho atoms can stabilize the H atoms on CuH facet (Figure S31). As shown in Figure 5a, it can be noticed that the adsorption energy of CO_2 on HoSA-CuH facet is negative (in contrast to the case for Cu(111)), which can facilitate the capture of CO_2 at the active sites on HoSA-CuH. Figure 5b clearly shows that the electrons of doped Ho atom on CuH facet can transfer to surrounding CuH facet, which can further enhance the electron cloud density on CuH facet. The electron transfer from the different doped rare-earth elements to Cu active site was discussed in Figure S32. Therefore, the electron cloud density on CuH facet is higher than on Cu(111) facet, thereby facilitating the CO_2 adsorption (Figure S33), which is in good agreement with Auger LMM spectra. For the critical step of *COOH formation (marked with a ☆ symbol in Figure 5a), it could be noted that the lattice hydrogen atom from HoSA-CuH participates the reaction, resulting in a much-lowered activation barrier. For the following step of *CO dimerization, the barrier for HoSA-CuH is only 0.92 eV, far lower than for Cu(111) (1.59 eV).[21] The significantly lowered energy barrier for the rate-determining step (RDS) in C–C coupling demonstrates a substantially optimized reaction pathway for CO_2-to-C_{2+} conversion, thus improving the selectivities for C_{2+} products.[22,38]

To further probe the key intermediate species for multi-carbon products involved in the electrocatalytic CO_2RR process over HoSA-CuH and Ho-free sample, we carried out in situ attenuated total reflection surface-enhanced infrared absorption spectroscopy (ATR-SEIRAS). A series of spectra were recorded for the two samples under potentials applied from 0 V to −2.0 V (vs. RHE). It was found that over the entire potential range, the signals characteristic of key intermediates could be identified under lower potentials over HoSA-CuH, indicative of a superior catalytic performance. As shown in Figures 5c and d, the peak near 2315 cm^{-1} for HoSA-CuH is attributed to the asymmetric stretching of adsorbed CO_2[51–54] whereas this peak is absent for Ho-free sample. Such a comparison implies that HoSA-CuH could enrich and thus activate CO_2 during the catalytic process, consistent with the DFT results that the electron-rich Cu atom would favor CO_2 activation (Figures 5a–5c). The peak at about 1400 cm^{-1} for both samples is attributed to *COOH intermediate.[55–58] The signal of *COOH over HoSA-CuH has a higher intensity than over Ho-free sample, suggesting that the key intermediate could readily form over the HoSA-CuH catalyst. A minor peak around 1080 cm^{-1} is attributed to $*OC_2H_5$.[59,60] In particular, the peaks at ∼1040 cm^{-1} for HoSA-CuH could be observed, associated with *COH, that is, the key intermediates from CO_2-to-C_{2+} conversion.[61] The peak around 1182 cm^{-1} can be ascribed to adsorbed *OCCOH intermediate, confirming the presence of C–C coupling over HoSA-CuH; in contrast, such peaks are absent for Ho-free sample.

In order to unveil the structural information of catalytic sites on HoSA-CuH for C–C coupling, operando XAFS spectra at Cu K-edge were recorded at t open-circuit potential (OCP, where the system remains unreacted), and a series of negative potentials (−1.50, −1.70, and − 1.90 V vs. RHE). As shown in Figure S34, the absorption edge for HoSA-CuH is located at higher energy under OCP, indicating a higher Cu valence state. With more negative potentials applied, the absorption edge shifts to lower energy, implying the decrease of the Cu valence state. The absorption edge was recovered after the applied potential was off, suggesting a good stability for HoSA-CuH. Notably, for all the test potentials, the absorption edges for HoSA-CuH are located between that for Cu and Cu_2O, suggesting that the Cu^0 and Cu^+ coexist in HoSA-CuH during the CO_2RR process, which has been known as a favorable structure to C–C coupling. From the analysis above, it can be determined that C–C coupling could readily proceed over HoSA-CuH, in good agreement with the DFT result of lower Gibbs energy for RDS in C–C coupling.

Interestingly, we noticed a peak around 1650 cm^{-1} in ATR-SEIRAS, which is attributed to water molecule bending. This peak becomes less intense as the potential goes more negative, implying that the conversion from H_2O to H_2 is suppressed. We further conducted deuterium (D) isotope labeling to identify the source of hydrogen for C_{2+} generation. The electrolyte was prepared using only D_2O (and K_2CO_3) and the electrolyte obtained after CO_2RR was

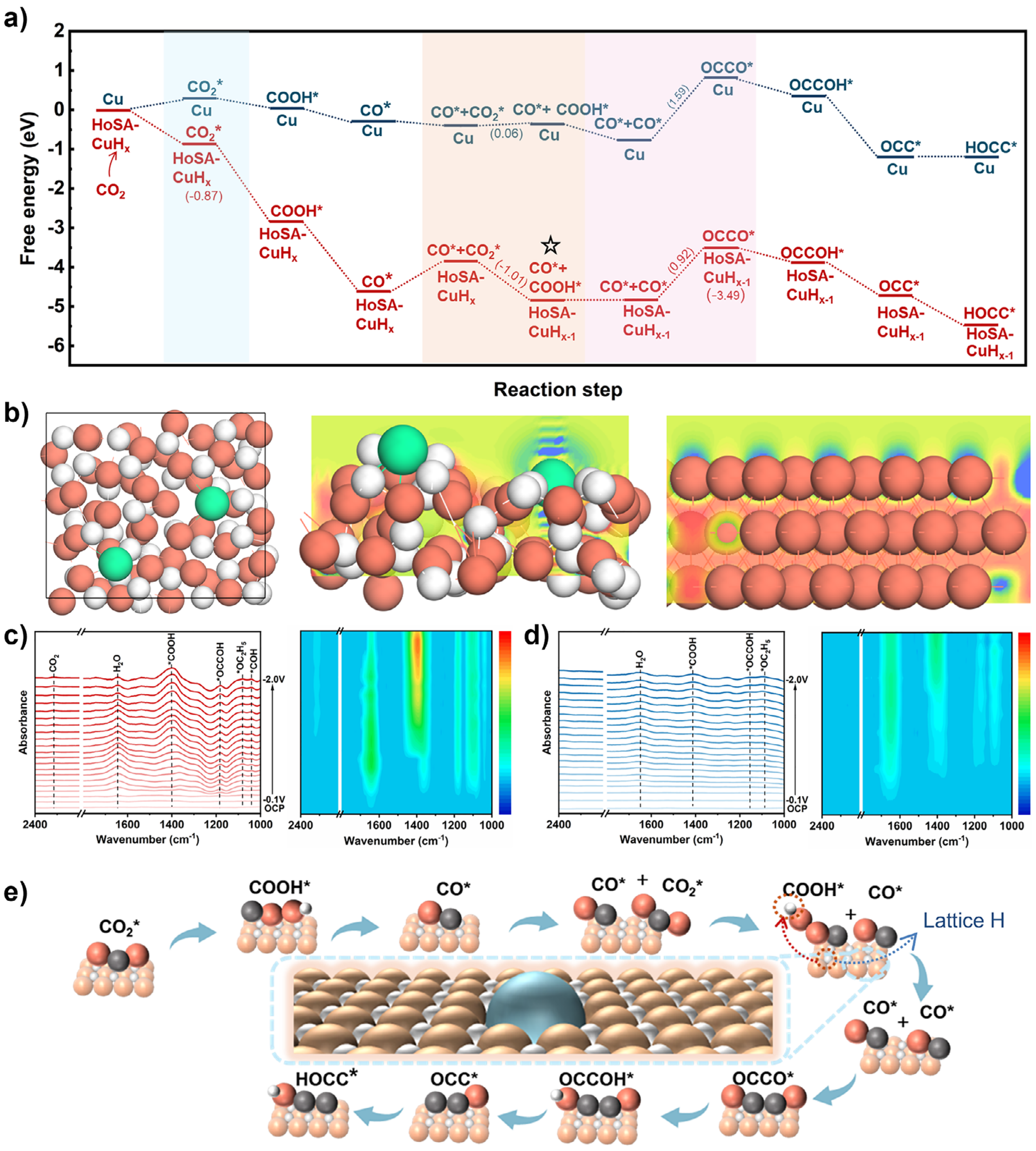

Figure 5. The reactive mechanism of the HoSA-CuH. a) The reaction energy diagram for the CO_2RR to C_2 intermedia on HoSA-CuH and Cu (111) facets via a direct *CO dimerization pathway. b) Structural model for HoSA-CuH (left), charge differential density map of HoSA-CuH (middle), and Cu (111) (right) facets. Orange, green, and white spheres stand for Cu, Ho, and H atoms, respectively. c and d) ATR-SEIRAS spectra on the surfaces and corresponding contour maps of HoSA-CuH and Ho-free catalysts. e) Proposed reaction scheme for CO_2 reduction to C_2 intermedia. Gray, pink, and white spheres stand for C, O, and H atoms, respectively.

subjected to gas chromatography–mass spectrometry (GC-MS). Figure S35 compares the signals of ethanol between the standard reference and the product obtained in our experiment; it could be noted that the electro synthesized ethanol molecules contain ^{1}H, which could only come from the HoSA-CuH sample itself. Therefore, we postulate that during CO_2RR, the lattice hydrogen atoms in CuH could participate in the reaction[62] via a Mars–van Krevelen mechanism[20] specifically, the reaction intermediates could combine with those active H species and the catalyst would subsequently recover (as evidenced in operando XAFS tests) by capturing free protons. As shown in Figure 5e, the reaction scheme of lattice hydrogen participation is proposed for CO_2 reduction to C_2 intermedia. To sum up, it could be inferred that the introduction of single Ho atoms could help stabilize the CuH phase, forming HoSA-CuH, the hydrogen atoms in which could participate in CO_2RR, thereby altering the reaction pathway and substantially lower the reaction barrier for C–C coupling[63] resulting in an improved selectivity for C_{2+} over a broad window of high current densities.

Conclusions

In this work, we developed a facile method for the preparation of CuH branched nanosheets doped with Ho single atoms (HoSA-CuH). The experimental characterizations show that the single-atomic Ho dopants could significantly enhance the stability of the CuH catalyst. Finite-element analyses reveal that the branched structure of HoSA-CuH leads to a high local CO_2 concentration due to mass transport acceleration and thus helps to alleviate the typical issue of CO_2 depletion under high current densities. At 700–1200 mA cm^{-2}, the selectivity for C_{2+} over HoSA-CuH is consistently above 80% and C_2 products (primarily ethylene and ethanol) account for 95% of all the C_{2+} products, and the competing HER is substantially suppressed. Under large variations in current density, the catalyst exhibits a high FE_{C2+} and a high durability. Compared with the best-performing catalysts reported thus far, our HoSA-CuH displays the broadest current density range for high FE_{C2+}. In situ spectroscopies (ATR-SEIRAS and operando XAFS) and DFT simulations reveal that the introduction of Ho single atoms leads to a higher electron density at the Cu surface, which is conducive to CO_2 enrichment and activation. The deuterium isotope labeling experiment confirm that the lattice hydrogen in CuH participate in the reaction, thereby lowering the energy barrier for the RDS in C–C coupling. This work demonstrates a high-efficiency catalyst for ampere-level CO_2 electroreduction, achieving a FE for C_{2+} above 80% over a wide variation range of current densities, thus offering a feasible solution to integrating CO_2RR with renewable energy technologies.

Acknowledgements

The work was financially supported by the National Key R&D Program of China (No. 2022YFA1502902), National Natural Science Foundation of China (No.52472236 and No.52072260, No.22531007), Tianjin Natural Science Foundation (25JCZDJC00770, 21JCZXJC00130), Natural Foundation of Liaoning Province (2024-MSBA-13), Research and Reform Project on Graduate Education of Tianjin University of Technology (YBXM2315). We acknowledge BL14W1 (https://cstr.cn/31124.02.SSRF.BL14W1), BL11B(https://cstr.cn/31124.02.SSRF.BL11B) and BL16U1 (https://cstr.cn/31124.02.SSRF.BL16U1) beamline of Shanghai Synchrotron Radiation Facility (SSRF) Shangha and 1W1B beamline of Beijing Synchrotron Radiation Facility (BSRF) Beijing (China) for providing the beam time. the Natural Foundation of Liaoning Province (2024-MSBA-13).

Conflict of Interests

The authors declare no conflict of interest.

Data Availability Statement

The data that support the findings of this study are available in the Supporting Information of this article.

Keywords: CO_2 electroreduction • Copper hydride • Finite-element analyses • Nanocrystal • Single-atom catalysts

---

[1] Z. Wei, W. Wang, T. Shao, S. Yang, C. Liu, D. Si, R. Cao, M. Cao, *Angew. Chem. Int. Ed.* **2025**, *64*, e202417066, https://doi.org/10.1002/anie.202417066.
[2] Y. Zhou, F. Che, M. Liu, C. Zou, Z. Liang, P. De Luna, H. Yuan, J. Li, Z. Wang, H. Xie, H. Li, P. Chen, E. Bladt, R. Quintero-Bermudez, T.-K. Sham, S. Bals, J. Hofkens, D. Sinton, G. Chen, E. H. Sargent, *Nat. Chem.* **2018**, *10*, 974–980, https://doi.org/10.1038/s41557-018-0092-x.
[3] J. Jiao, Y. Ma, X. Han, A. Ergu, C. Zhang, P. Chen, W. Liu, Q. Luo, Z. Shi, H. Xu, C. Chen, Y. Li, T. Lu, *Nat. Commun.* **2025**, *16*, 857. https://doi.org/10.1038/s41467-025-56101-8.
[4] J. Kok, P. P. Albertini, J. Leemans, R. Buonsanti, T. Burdyny, *Nat. Rev. Mater.* **2025**, *10*, 550–563, https://doi.org/10.1038/s41578-025-00815-0.
[5] Y. Yang, W. Zhang, G. Wu, Q. Huang, J. Wen, D. Wang, M. Liu, *Angew. Chem. Int. Ed.* **2025**, *64*, e202504423, https://doi.org/10.1002/anie.202504423.
[6] Y. Guan, Y. Li, Z. Li, Y. Hou, L. Lei, B. Yang, *Adv. Mater.* **2025**, *37*, 2417567, https://doi.org/10.1002/adma.202417567.
[7] Z. Niu, L. Chi, Z. Wu, P. Yang, M. Fan, M. Gao, *Nat. Sci. Open* **2023**, *2*, 20220044.
[8] J. Shen, D. Wang, *Nano Res. Energy*. **2024**, *3*, e9120096.
[9] L.-P. Chi, Y.-C. Zhang, Z.-Z. Niu, X.-L. Zhang, Y.-C. Li, T.-Y. Zhang, S.-P. Sun, P.-G. Lu, K.-B. Tang, M.-R. Gao, *Angew. Chem. Int. Ed.* **2025**, *64*, e202503539, https://doi.org/10.1002/anie.202503539.
[10] H. Deng, T. Liu, W. Zhao, J. Wang, Y. Zhang, S. Zhang, Y. Yang, C. Yang, W. Teng, Z. Chen, G. Zheng, F. Li, Y. Su, J. Hui, Y. Wang, *Nat. Commun.* **2024**, *15*, 9706. https://doi.org/10.1038/s41467-024-54107-2.
[11] J.-M. McGregor, J. T. Bender, A. S. Petersen, L. Cañada, J. Rossmeisl, J. F. Brennecke, J. Resasco, *Nat. Catal.* **2025**, *8*, 79–91, https://doi.org/10.1038/s41929-024-01278-2.
[12] C. J. Bondue, M. Graf, A. Goyal, M. T. M. Koper, *J. Am. Chem. Soc.* **2021**, *143*, 279–285, https://doi.org/10.1021/jacs.0c10397.
[13] Q. Wang, H. Wei, P. Liu, Z. Su, X.-Q. Gong, *Nano Res. Energy*. **2024**, *3*, e9120112.
[14] J.-W. DuanMu, Z.-Z. Wu, F.-Y. Gao, P.-P. Yang, Z.-Z. Niu, Y.-C. Zhang, L.-P. Chi, M.-R. Gao, *Prec. Chem.* **2024**, *2*, 151–160, https://doi.org/10.1021/prechem.4c00002.
[15] X. Kong, C. Wang, H. Zheng, Z. Geng, J. Bao, J. Zeng, *Sci. China Chem.* **2021**, *64*, 1096–1102, https://doi.org/10.1007/s11426-020-9934-0.
[16] W. Ma, S. Xie, T. Liu, Q. Fan, J. Ye, F. Sun, Z. Jiang, Q. Zhang, J. Cheng, Y. Wang, *Nat. Catal.* **2020**, *3*, 478–487, https://doi.org/10.1038/s41929-020-0450-0.
[17] L. Ding, N. Zhu, Y. Hu, Z. Chen, P. Song, T. Sheng, Z. Wu, Y. Xiong, *Angew. Chem. Int. Ed.* **2022**, *61*, e202209268, https://doi.org/10.1002/anie.202209268.

[18] J. Li, Y. Chen, B. Yao, W. Yang, X. Cui, H. Liu, S. Dai, S. Xi, Z. Sun, W. Chen, Y. Qin, J. Wang, Q. He, C. Ling, D. Wang, Z. Zhang, *J. Am. Chem. Soc.* **2024**, *146*, 5693–5701, https://doi.org/10.1021/jacs.4c00475.

[19] P. Wang, H. Yang, C. Tang, Y. Wu, Y. Zheng, T. Cheng, K. Davey, X. Huang, S. Z. Qiao, *Nat. Commun.* **2022**, *13*, 3754. https://doi.org/10.1038/s41467-022-31427-9.

[20] D. L. Meng, M. D. Zhang, D. H. Si, M. J. Mao, Y. Hou, Y. B. Huang, R. Cao, *Angew. Chem. Int. Ed.* **2021**, *60*, 25485–25492, https://doi.org/10.1002/anie.202111136.

[21] J. Feng, L. Wu, S. Liu, L. Xu, X. Song, L. Zhang, Q. Zhu, X. Kang, X. Sun, B. Han, *J. Am. Chem. Soc.* **2023**, *145*, 9857–9866, https://doi.org/10.1021/jacs.3c02428.

[22] E. W. Lees, J. C. Bui, O. Romiluyi, A. T. Bell, A. Z. Weber, *Nat. Chem. Eng.* **2024**, *1*, 340–353, https://doi.org/10.1038/s44286-024-00062-0.

[23] M. McKee, M. Kutter, Y. Wu, H. Williams, M. A. Vaudreuil, M. Carta, A. K. Yadav, H. Singh, J. F. O. Masson, D. Lentz, M. F. Kühnel, N. Kornienko, *Nat. Chem.* **2025**, *17*, 92–100, https://doi.org/10.1038/s41557-024-01650-6.

[24] J. Feng, L. Wu, X. Song, L. Zhang, S. Jia, X. Ma, X. Tan, X. Kang, Q. Zhu, X. Sun, B. Han, *Nat. Commun.* **2024**, *15*, 4821. https://doi.org/10.1038/s41467-024-49308-8.

[25] Y. Guan, H. Wen, K. Cui, Q. Wang, W. Gao, Y. Cai, Z. Cheng, Q. Pei, Z. Li, H. Cao, T. He, J. Guo, P. Chen, *Nat. Chem.* **2024**, *16*, 373–379, https://doi.org/10.1038/s41557-023-01395-8.

[26] Z. Shi, C. Zhang, H. Wang, Z. Ji, M. Qi, S. Liu, W. Wang, C. Chen, J. Jiao, T. Lu, *Appl. Catal. B Environ.* **2026**, *380*, 125745, https://doi.org/10.1016/j.apcatb.2025.125745.

[27] Z.-H. Zhao, D. Ren, *Angew. Chem. Int. Ed.* **2025**, *64*, e202415590, https://doi.org/10.1002/anie.202415590.

[28] Y. Song, X. Zhang, Z. Xiao, Y. Wang, P. Yi, M. Huang, L. Zhang, *Appl. Catal. B Environ.* **2024**, *352*, 124028, https://doi.org/10.1016/j.apcatb.2024.124028.

[29] N. Sun, S. Ru, C. Zhang, W. Liu, Q. Luo, J. Jiao, T. Lu, *Fundam. Res.* **2025**, *5*, 1488–1494, https://doi.org/10.1016/j.fmre.2022.07.014.

[30] S. Xie, S. Tian, J. Yang, N. Wang, Q. Wan, M. Wang, J. Liu, J. Zhou, P. Qi, K. Sui, X. Li, D. Ma, X. S. Zhao, *Angew. Chem. Int. Ed.* **2025**, *64*, e202424316, https://doi.org/10.1002/anie.202424316.

[31] J. Jiao, Q. Yuan, M. Tan, X. Han, M. Gao, C. Zhang, X. Yang, Z. Shi, Y. Ma, H. Xiao, J. Zhang, T. Lu, *Nat. Commun.* **2023**, *14*, 6164. https://doi.org/10.1038/s41467-023-41863-w.

[32] P. P. Albertini, M. A. Newton, M. Wang, O. Segura Lecina, P. B. Green, D. C. Stoian, E. Oveisi, A. Loiudice, R. Buonsanti, *Nat. Mater.* **2024**, *23*, 680–687, https://doi.org/10.1038/s41563-024-01819-x.

[33] J. Liu, P. Li, J. Bi, S. Jia, Y. Wang, X. Kang, X. Sun, Q. Zhu, B. Han, *J. Am. Chem. Soc.* **2023**, *145*, 23037–23047, https://doi.org/10.1021/jacs.3c05562.

[34] Y. Lu, F. Yue, T. Liu, Y.-C. Huang, F. Fu, Y. Jing, H. Yang, C. Yang, *Nat. Commun.* **2025**, *16*, 2392. https://doi.org/10.1038/s41467-025-57097-x.

[35] Y. Wang, F. Yang, H. Xu, J. Jang, E. P. Delmo, X. Qiu, Z. Ying, P. Gao, S. Zhu, M. D. Gu, M. Shao, *Angew. Chem. Int. Ed.* **2024**, *63*, e202400952, https://doi.org/10.1002/anie.202400952.

[36] K. Huang, K. Tang, M. Wang, Y. Wang, T. Jiang, M. Wu, *Adv. Funct. Mater.* **2024**, *34*, 2315324, https://doi.org/10.1002/adfm.202315324.

[37] J. An, S. Ge, G. Wang, H. Fu, *Energy Environ. Sci.* **2024**, *17*, 5039–5047. https://doi.org/10.1039/D4EE00572D.

[38] Q. Wu, R. Du, P. Wang, G. I. N. Waterhouse, J. Li, Y. Qiu, K. Yan, Y. Zhao, W. W. Zhao, H. J. Tsai, M. C. Chen, S.-F. Hung, X. Wang, G. Chen, *ACS Nano* **2023**, *17*, 12884–12894, https://doi.org/10.1021/acsnano.3c04951.

[39] X. Lv, Q. Liu, J. Wang, X. Wu, X. Li, Y. Yang, J. Yan, A. Wu, H. B. Wu, *Appl. Catal. B Environ.* **2023**, *324*, 122272, https://doi.org/10.1016/j.apcatb.2022.122272.

[40] Y. Jiang, C. Lv, B. Lu, Y. Song, T. Liu, X. Zhang, D. Gao, K. Ye, G. Wang, *ACS Nano* **2025**, *19*, 11263–11272, https://doi.org/10.1021/acsnano.4c18967.

[41] X. Chen, S. Jia, J. Zhai, J. Jiao, M. Dong, C. Xue, T. Deng, H. Cheng, Z. Xia, C. Chen, X. Xing, J. Zeng, H. Wu, M. He, B. Han, *Nat. Commun.* **2024**, *15*, 7691. https://doi.org/10.1038/s41467-024-51928-z.

[42] R. Chen, Y. Jiang, Y. Zhu, L. Zhang, Y. Li, C. Li, *Adv. Funct. Mater.* **2025**, *35*, 2415940, https://doi.org/10.1002/adfm.202415940.

[43] M. Zheng, P. Wang, X. Zhi, K. Yang, Y. Jiao, J. Duan, Y. Zheng, S.-Z. Qiao, *J. Am. Chem. Soc.* **2022**, *144*, 14936–14944, https://doi.org/10.1021/jacs.2c06820.

[44] J. Liu, P. Li, S. Jia, Y. Wang, L. Jing, Z. Liu, J. Zhang, Q. Qian, X. Kang, X. Sun, Q. Zhu, B. Han, *Nat. Synth.* **2025**, *4*, 730–743, https://doi.org/10.1038/s44160-025-00752-4.

[45] Y. Cao, S. Chen, S. Bo, W. Fan, J. Li, C. Jia, Z. Zhou, Q. Liu, L. Zheng, F. Zhang, *Angew. Chem. Int. Ed.* **2023**, *62*, e202303048.

[46] T. Hou, J. Zhu, H. Gu, X. Li, Y. Sun, Z. Hua, R. Shao, C. Chen, B. Hu, L. Mai, S. Chen, D. Wang, J. Zhang, *Angew. Chem. Int. Ed.* **2025**, *64*, e202424749, https://doi.org/10.1002/anie.202424749.

[47] W. Zhang, S. Zhao, X. Wang, L. Yang, Q. Zhao, C. Jiang, Y. Wang, Y. Wu, Y. Chen, *ACS Nano* **2025**, *19*, 24023–24033, https://doi.org/10.1021/acsnano.5c06395.

[48] D. Zhou, C. Chen, Y. Zhang, M. Wang, S. Han, X. Dong, T. Yao, S. Jia, M. He, H. Wu, B. Han, *Angew. Chem. Int. Ed.* **2024**, *63*, e202400439.

[49] H. Cai, H. Yang, D. Li, S. He, X. Zhang, Q. Hu, C. He, *Angew. Chem. Int. Ed.* **2025**, *64*, e202425325.

[50] L. Fan, F. Li, T. Liu, J. E. Huang, R. K. Miao, Y. Yan, S. Feng, C.-W. Tai, S.-F. Hung, H.-J. Tsai, M.-C. Chen, Y. Bai, D. Kim, S. Park, P. Papangelakis, C. Wu, A. Shayesteh Zeraati, R. Dorakhan, L. Sun, D. Sinton, E. Sargent, *Nat. Synth.* **2025**, *4*, 262–270, https://doi.org/10.1038/s44160-024-00689-0.

[51] S. Chen, X. Zheng, P. Zhu, Y. Li, Z. Zhuang, H. Wu, J. Zhu, C. Xiao, M. Chen, P. Wang, D. Wang, Y.-L. He, *Angew. Chem. Int. Ed.* **2024**, *63*, e202411591, https://doi.org/10.1002/anie.202411591.

[52] M. Qi, Y. Ma, C. Zhang, B. Li, X. Yang, Z. Shi, S. Liu, C. An, J. Jiao, T. Lu, *Sci. China Chem.* **2025**, *68*, 1620–1626, https://doi.org/10.1007/s11426-024-2307-y.

[53] L. Zhang, J. Feng, L. Wu, X. Ma, X. Song, S. Jia, X. Tan, X. Jin, Q. Zhu, X. Kang, J. Ma, Q. Qian, L. Zheng, X. Sun, B. Han, *J. Am. Chem. Soc.* **2023**, *145*, 21945–21954, https://doi.org/10.1021/jacs.3c06697.

[54] Y. Katayama, F. Nattino, L. Giordano, J. Hwang, R. R. Rao, O. Andreussi, N. Marzari, Y. Shao-Horn, *The J. Phys. Chem. C* **2019**, *123*, 5951–5963, https://doi.org/10.1021/acs.jpcc.8b09598.

[55] F. Ma, P. Zhang, X. Zheng, L. Chen, Y. Li, Z. Zhuang, Y. Fan, P. Jiang, H. Zhao, J. Zhang, Y. Dong, Y. Zhu, D. Wang, Y. Wang, *Angew. Chem. Int. Ed.* **2024**, *63*, e202412785, https://doi.org/10.1002/anie.202412785.

[56] J. Cheng, L. Chen, Y. Zhang, M. Wang, Z. Zheng, L. Jiang, Z. Deng, Z. Wei, M. Ma, L. Xiong, W. Hua, D. Song, W. Huo, Y. Lian, W. Yang, F. Lyu, Y. Jiao, Y. Peng, *Nat. Commun.* **2025**, *16*, 3743. https://doi.org/10.1038/s41467-025-59025-5.

[57] H.-L. Zhu, J.-R. Huang, M.-D. Zhang, C. Yu, P. Q. Liao, X.-M. Chen, *J. Am. Chem. Soc.* **2024**, *146*, 1144–1152, https://doi.org/10.1021/jacs.3c12423.

[58] X.-F. Qiu, H.-L. Zhu, J.-R. Huang, P.-Q. Liao, X. M. Chen, *J. Am. Chem. Soc.* **2021**, *143*, 7242–7246, https://doi.org/10.1021/jacs.1c01466.

[59] Y. Shi, J. Li, Z. Min, X. Wang, M. Hou, H. Ma, Z. Zhuang, Y. Qin, Y. Sun, D. Wang, Z. Zhang, *Sci. China Mater.* **2025**, *68*, 173–179.

[60] C. Guo, Y. Guo, Y. Shi, X. Lan, Y. Wang, Y. Yu, B. Zhang, *Angew. Chem. Int. Ed.* **2022**, *61*, e202205909, https://doi.org/10.1002/anie.202205909.

[61] C. Liu, M. Wang, J. Ye, L. Liu, L. Li, Y. Li, X. Huang, *Nano Lett.* **2023**, *23*, 1474–1480, https://doi.org/10.1021/acs.nanolett.2c04911.

[62] J. Li, W. Yu, H. Yuan, Y. Wang, Y. Chen, D. Jiang, T. Wu, K. Song, X. Jiang, H. Liu, R. Hu, M. Huang, W. Zhou, *Nat. Commun.* **2024**, *15*, 9499. https://doi.org/10.1038/s41467-024-53833-x.

[63] M. Wang, M. Fang, Y. Liu, C. Chen, Y. Zhang, S. Jia, H. Wu, M. He, B. Han, *J. Am. Chem. Soc.* **2025**, *147*, 16450–16458, https://doi.org/10.1021/jacs.5c03057.

Manuscript received: August 22, 2025
Revised manuscript received: October 21, 2025
Manuscript accepted: November 11, 2025
Version of record online: ■■, ■■